POLITECNICO DI TORINO
Repository ISTITUZIONALE

Facilely synthesized nitrogen-doped reduced graphene oxide functionalized with copper ions as electrocatalyst for oxygen reduction

Original
Facilely synthesized nitrogen-doped reduced graphene oxide functionalized with copper ions as electrocatalyst for oxygen reduction / Garino, N., Zeng, J., Castellino, M., Sacco, A., Risplendi, F., Fiorentin, M.R., Bejtka, K., Chiodoni, A., Salomon, D., Segura-Ruiz, J., Pirri, C.F., Cicero, G.. - In: NPJ 2D MATERIALS AND APPLICATIONS. - ISSN 2397-7132. - ELETTRONICO. - 5:2(2021). [10.1038/s41699-020-00185-x]

Availability:
This version is available at: 11583/2859772 since: 2021-01-06T17:57:26Z

Publisher:
Springer Nature

Published
DOI:10.1038/s41699-020-00185-x

Terms of use:

This article is made available under terms and conditions as specified in the corresponding bibliographic description in the repository

Publisher copyright

(Article begins on next page)

14 September 2026

npj | 2D Materials and Applications

www.nature.com/npj2dmaterials

ARTICLE OPEN

Check for updates

Facilely synthesized nitrogen-doped reduced graphene oxide functionalized with copper ions as electrocatalyst for oxygen reduction

Nadia Garino[1,2,4✉], Juqin Zeng[2,4✉], Micaela Castellino[1,2], Adriano Sacco[2], Francesca Risplendi[1], Michele Re Fiorentin[2], Katarzyna Bejtka[2], Angelica Chiodoni[2], Damien Salomon[3], Jaime Segura-Ruiz[3], Candido F. Pirri[1,2] and Giancarlo Cicero[1]

Nitrogen-doped reduced graphene oxide is successfully synthesized and functionalized with hydroxylated copper ions via one-pot microwave-assisted route. The presence of cationic Cu coordinated to the graphene layer is fully elucidated through a set of experimental characterizations and theoretical calculations. Thanks to the presence of these hydroxyl-coordinated Cu^{2+} active sites, the proposed material shows good electrocatalytic performance for the oxygen reduction reaction, as evidenced by an electron transfer number of almost 4 and by high onset and half-wave potentials of 0.91 V and 0.78 V vs. the reversible hydrogen electrode, respectively. In addition, the N-doped Cu-functionalized graphene displays a superior current retention with respect to a commercial Pt/C catalyst during the stability test, implying its potential implementation in high-performance fuel cells and metal-air batteries.

npj 2D Materials and Applications (2021)5:2 ; https://doi.org/10.1038/s41699-020-00185-x

INTRODUCTION

To date, several efficient and smart technologies for energy conversion and storage are emerging as suitable strategies to build a green and sustainable future. Among them, fuel cells[1,2] and metal-air batteries[3,4] attract particular worldwide interest, due to their high energy density, enabling an increasing driving autonomy in electric vehicles, to be comparable to that of gasoline-supplied vehicles, and supporting the development of small advanced portable electronic devices as well as auxiliary power units[5]. However, both these electrochemical devices suffer from kinetically sluggish oxygen reduction reaction (ORR) at the oxygen/air cathode[6,7]. In order to boost ORR for practical and large-scale applications, active, stable and low-cost electrocatalysts are highly desirable. During the last decades, extensive efforts have been focused on the discovery and development of such ORR active materials[8–12].

Among many platinum group metal-free catalysts, carbon-based materials, doped with heteroatoms and/or transition metals, are considered the most promising alternatives to the state-of-the-art platinum-based catalysts for ORR due to their encouraging performance[13–16]. In particular, many research groups reported heteroatom-doped graphene, such as nitrogen-doped[17,18], boron-doped[19], sulfur-doped[20], phosphorous-doped[21], and edge-halogenated (Cl, Br or I) graphene[22], as efficient and robust ORR electrocatalyst[23]. Moreover, graphene materials with binary, ternary and quaternary doping of various heteroatoms were also widely investigated as ORR catalysts, such as boron/nitrogen-doped[24], nitrogen/sulfur-doped[25], nitrogen/phosphorous-doped[26,27], nitrogen/boron/phosphorous-doped[28] and boron/nitrogen/phosphorus/sulfur-doped graphene[29].

To date, incorporating metal sites into graphene-based materials is considered an effective strategy to further improve the catalytic performance toward ORR[30–35]. In biological systems, copper centers (Cu^{2+}), such as those present in cytochrome c oxidase and laccase, can bind molecular oxygen and efficiently reduce it to water. Taking the cue from nature, Wang et al.[36] reported a bioinspired catalyst, with the coexistence of Cu^0 and Cu^{2+} connected to N atoms in reduced graphene oxide (rGO), exhibiting superior catalytic activity (onset potential 0.978 V vs. the reversible hydrogen electrode (RHE) and electron transfer number in the range from 3.7 to 4) with respect to conventional Pt/C in alkaline media. Shakhseh et al.[30] studied sulfur and copper modified graphene, showing an onset potential of 1.09 V vs. RHE and a high selectivity for the four-electron ORR. Li et al.[37] reported single atomic Cu anchored to an ultrathin two-dimensional carbon matrix, demonstrating impressive ORR activity, with an electron transfer number of 3.97 and a half-wave potential of 0.869 V vs. RHE. Despite the remarkable ORR activity, it is worth noticing that most of the above-mentioned doped and Cu-modified graphene catalysts were prepared through pyrolysis and thermal annealing at high temperatures, which are time- and energy-consuming.

In this work, we propose to achieve surface functionalization of N-doped rGO with active copper ions through a simple and fast route with microwave irradiation, using graphene oxide (GO), urea and copper sulfate as chemical precursors. Under microwave radiation at 180 °C, GO was reduced and N atoms were simultaneously bonded to the graphitic lattice, forming N-doped rGO (denoted as N-rGO in this work). With the addition of copper precursor, the metal ions are forced to bind to the residual oxygen-containing functional groups present at the rGO surface, generating additional catalytic Cu active sites for ORR on the carbonaceous N-rGO. This sample is indicated as Cu-N-rGO. The prepared materials were carefully characterized utilizing field emission scanning electron microscopy (FESEM), transmission electron microscopy (TEM) and X-ray photoelectron spectroscopy (XPS). Thanks to the comparison between experimental and

[1]Applied Science and Technology Department, Politecnico di Torino, Corso Duca degli Abruzzi 24, 10129 Torino, Italy. [2]Center for Sustainable Future Technologies @Polito, Istituto Italiano di Tecnologia, Via Livorno 60, 10144 Torino, Italy. [3]ESRF – The European Synchrotron, Avenue des Martyrs 71, 38000 Grenoble, France. [4]These authors contributed equally: Nadia Garino, Juqin Zeng. ✉email: nadia.garino@polito.it; juqin.zeng@iit.it

simulated extended X-ray absorption fine structure (EXAFS) spectra with density functional theory (DFT) calculations, the molecular structure responsible for the high electrocatalytic activity of this complex toward ORR has been identified and characterized. Various electrochemical techniques were employed to evaluate the activity and durability of the electrocatalysts for ORR in atmospheric environment in alkaline solution. The Cu-N-rGO demonstrated superior catalytic activity to the counterpart N-rGO, and enhanced durability compared to commercial Pt/C.

RESULTS

Physical and chemical characterizations

FESEM and TEM characterizations were performed to evaluate the morphology and structural properties of the as prepared Cu-N-rGO samples (see Fig. 1). FESEM images (Fig. 1a, b) show that the obtained flakes exhibit smooth surfaces, large area, and are easily found well spread over the surface. They exhibit the characteristic morphology of the 2-dimensional graphene structure, with no modification or damage induced to the original GO by the preparation technique. This is also confirmed by TEM characterization. Bright field TEM (BFTEM) (Fig. 1c) and scanning TEM (STEM) (Fig. 1d, e) images confirm the good quality of the obtained rGO, and at the same time show that no copper oxide particles or metallic aggregates are present. The selected area electron diffraction pattern, shown in Fig. 1f, presents a well-defined spot pattern, composed of elongated bright spots in a hexagonal configuration. This corresponds to rGO in [001] axis zone; the points are elongated because the signal is generated by a small number of stacked rGO layers. There is no detectable evidence of copper in the form of metallic phase or other solid compounds, since no discrete spots or rings appear in the diffraction pattern; consistently, the interplanar spacings are unchanged with respect to those observed in pristine rGO. However, the presence of copper in these samples was confirmed by energy dispersive X-ray spectroscopy (EDX) (shown in Fig. 1g): signals from C, O, N, Cu, Si and Au (the last two being due to the experimental set-up) were detected in the area where no particles or aggregation was observed.

Semi-quantitative elemental analysis was achieved via XPS measurements. The survey spectrum (see Fig. 2a) highlights the presence of C (77.5 at.%), O (17.2 at.%), N (2.4 at.%) and Cu (2.2 at.%), and traces of S, Cl, Na (<0.4 at.%) due to precursors. To search for specific signals induced by the presence of Cu atoms in the rGO matrix, we compared the N-rGO high resolution (HR) spectra to those of the Cu-N-rGO. C 1s HR spectra (see Supplementary Fig. 1a) were normalized and overlapped, and showed no substantial changes. This suggests that Cu atoms are not bonded directly to C atoms, since no perturbation to their chemical environment is detectable. The C 1s deconvolution procedure applied to Cu-N-rGO sample (see Fig. 2b) shows the well-known peaks due to sp^2 carbon, three peaks due to carbon oxygen/nitrogen bonds and the $\pi-\pi^*$ shake up satellite[38]. Performing a comparable analysis for the N 1s peak (see Supplementary Fig. 1b), we achieved the same conclusion obtained for the C 1s peak: no distortions are visible in the curves of the two samples. From N 1s deconvolution procedure applied to the HR spectra of both N-rGO and Cu-N-rGO, we obtained two components that can be assigned to N atoms implanted in the graphene lattice, one is attributed to pyrrolic-like nitrogen (399.1–399.6 eV) and the other is due to a quaternary or graphitic configuration (400.9–401.7 eV), as already reported in our previous work[9]. We can, therefore, state that N atoms are not involved into bonding with Cu either, differently from what observed for N and Mn in our previous work[33].

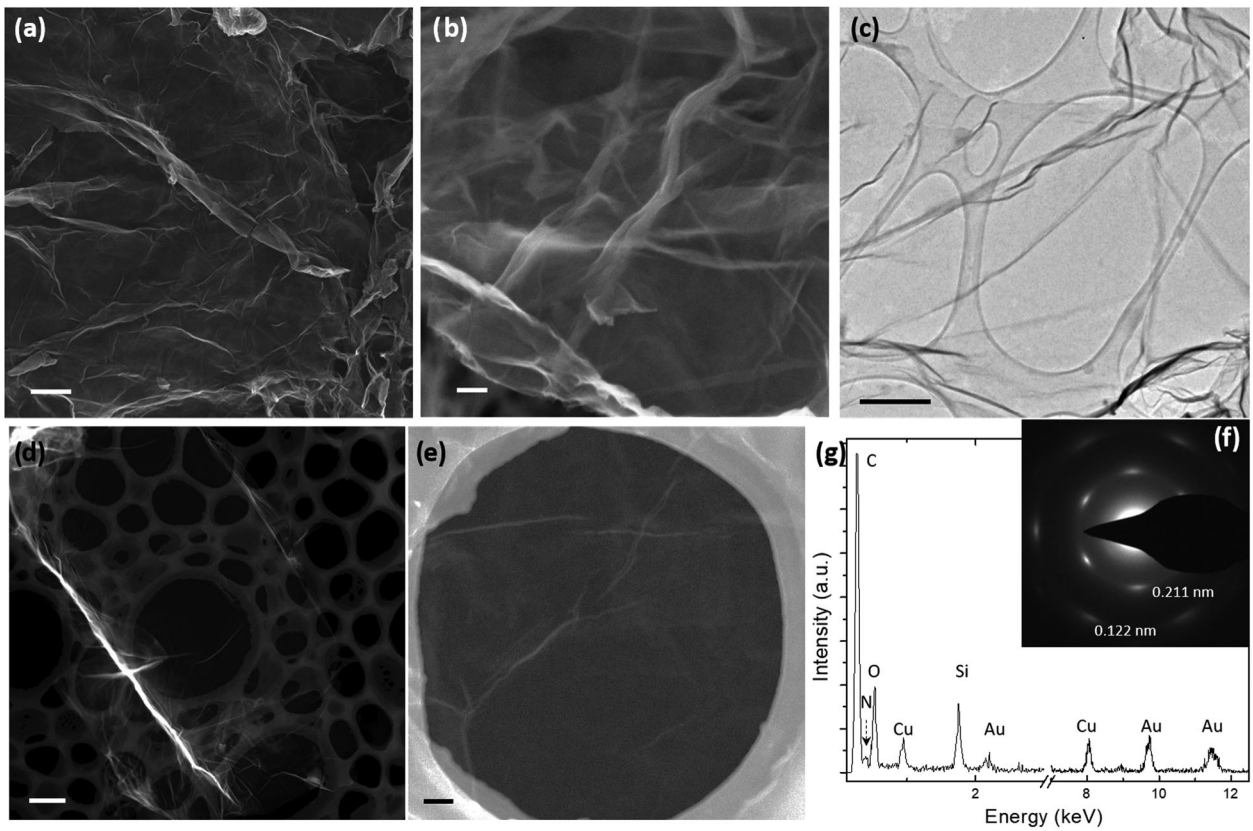

Fig. 1 Electron microscopy characterization of Cu-N-rGO sample. a FESEM micrograph (scale bar: 1 µm), **b** FESEM micrograph (scale bar: 100 nm), **c** BFTEM image (scale bar: 500 nm), **d** STEM micrograph (scale bar: 1 µm), **e** STEM micrograph (scale bar: 100 nm), **f** selected area electron diffraction pattern and **g** EDX spectrum.

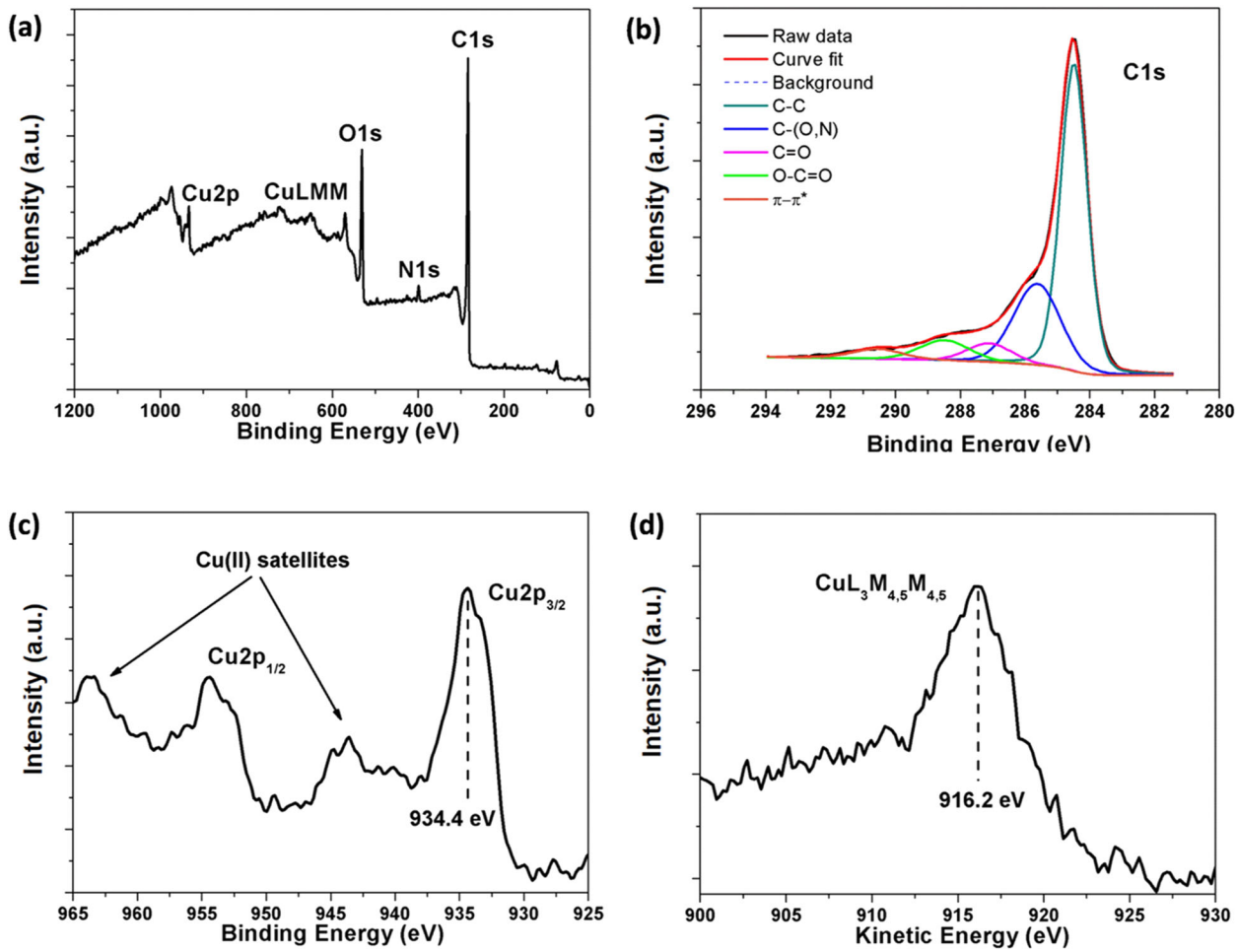

Fig. 2 XPS characterization of Cu-N-rGO sample. a Survey spectrum, **b** C 1s HR spectrum with deconvolution procedure, **c** Cu 2p HR doublet and **d** CuLMM Auger peak.

The Cu 2p doublet (Fig. 2c) presents the fingerprint typical of Cu(II) oxidation state which corresponds to the shake-up satellite located at 940–945 eV. Moreover, the $Cu2p_{3/2}$ peak maximum at 934.4 eV, slightly shifted towards higher binding energies compared to CuO bond (933.6 eV), can be attributed to $Cu(OH)_2$ chemical shift[39]. For a further confirmation, we analyzed the $CuL_3M_{4,5}M_{4,5}$ Auger peak (see Fig. 2d): the position of its maximum at 916.2 eV (in the kinetic energy scale) is in accordance with the values reported in the literature above mentioned. Moreover, the modified Auger parameter, calculated using the $Cu2p_{3/2}$ and $CuL_3M_{4,5}M_{4,5}$ peak positions and equal to 1850.6 eV, represents a further confirmation of our attribution to $Cu(OH)_2$ chemical shift. O 1 s HR spectrum (Supplementary Fig. 1c) has also been analyzed to confirm the presence of $Cu(OH)_2$ component. The fitting procedure results are: a first peak at 531.2 eV due to both –C–O and $Cu(OH)_2$ bonds, a second peak at 533.1 eV due to –C=O bond and a third flat one at binding energy higher than 534 eV ascribed to adsorbed H_2O[40]. In summary, from XPS results, we can state that Cu atoms, in a +2 oxidation state, are supposed to be bonded to OH group.

DFT and EXAFS

Starting from these experimental evidences, we employed DFT calculations to propose realistic structures where Cu^{2+} ions form ionic coordinated complexes, in which copper is bonded with the oxygen atoms of the functional groups (epoxides and hydroxides) present on rGO basal plane and hydroxyl groups originating from the synthesis solution. We built several model systems to represent our Cu-based samples: in some structures the Cu ion is coordinated to surface $-O^-$ groups (structures (a)–(b) of Fig. 3), or to surface epoxide groups only (structure (d) of Fig. 3), while in other structures it is also bound to hydroxyl groups (structures (c)–(f) of Fig. 3). All the structures depicted in Fig. 3 are characterized by a cell with null total charge ($q = 0$), except for structure (f) for which q is equal to -2. In all the simulated systems, the Cu ion oxidation state is equal to +2, as evaluated by XPS.

Upon structural relaxation, Cu binds to two or more O atoms at a bond distance of about 1.85 Å in case of OH group and about 1.90 Å in case of surface epoxides. To evaluate the stability of these Cu^{2+} based complexes, we calculated the binding energy (BE) between the complex and the rGO matrix (structures in Fig. 3), defined as the difference between the total energy of the interacting systems and those of the isolated components. The calculated BEs for the structures presented in Fig. 3 are lower than −1 eV for Cu^{2+} based complexes. We found that the most favorable structure, characterized by a high value of binding energy (−1.45 eV), is the one reported in Fig. 3f. These results demonstrate that Cu^{2+} ions bind to the rGO layer through the formation of metal complexes involving hydroxyl and epoxide groups, consistently with the XPS results that points at the presence of Cu^{2+} ions bound with O atoms only.

In order to determine the local structure around the Cu atoms in the Cu-N-rGO sample, EXAFS data around the K-edge of this element were acquired at the ID16-B beamline of the ESRF[41]. The data analysis was carried out comparing the experimental EXAFS

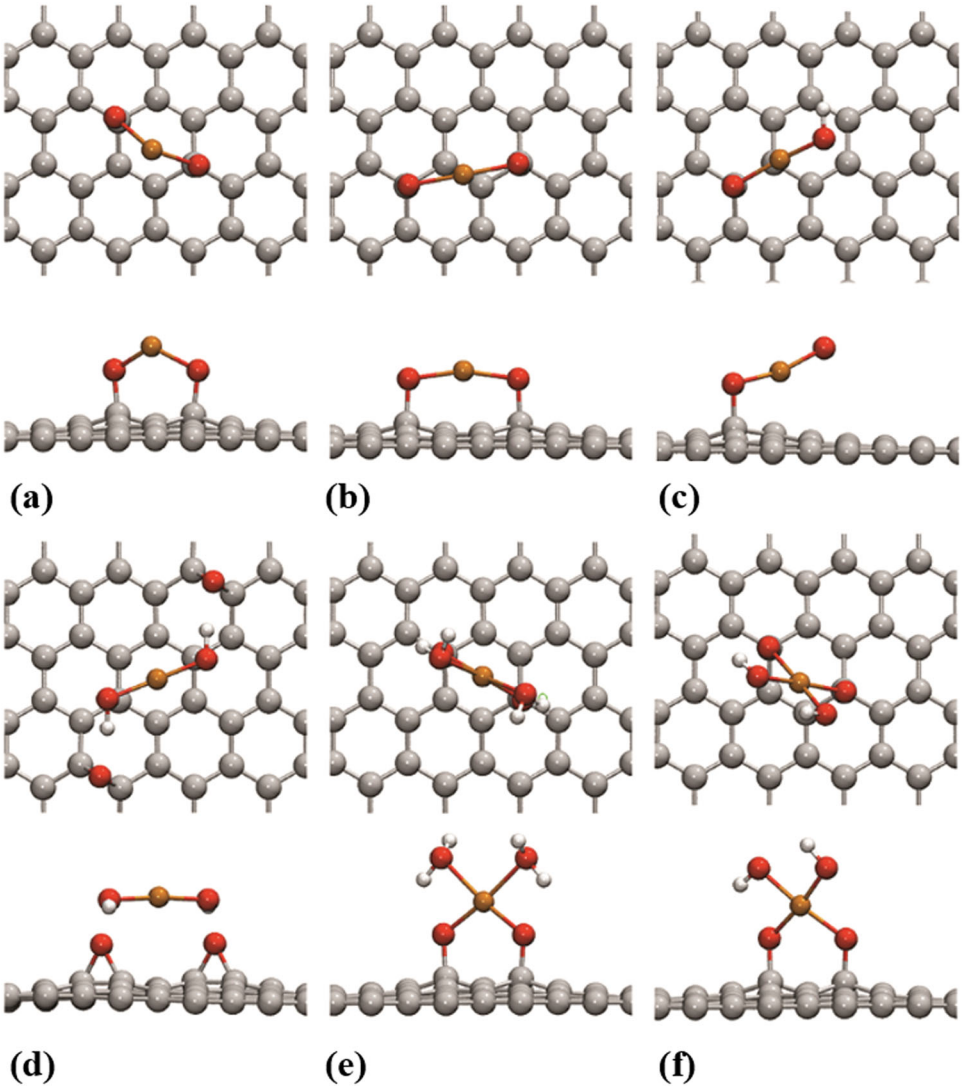

Fig. 3 Ball and stick representation of Cu-N-rGO structures. a, **b** Cu ion is coordinated to two surface $-O^-$ groups, **c** Cu ion is coordinated to one surface $-O^-$ group and also bound to one hydroxyl group, **d** Cu ion is coordinated to two surface epoxide groups, **e**, **f** Cu ion is coordinated to two surface $-O^-$ groups and also bound to hydroxyl groups. Gray spheres represent C atoms, red spheres O atoms, white spheres H atoms and orange spheres Cu atoms.

spectrum to the one obtained by simulating with the FEFF code[42] the spectra of the structures proposed by the ab initio modeling. Theoretical backscattering amplitudes and phase shifts for all single and multiple scattering paths were calculated for the different Cu-N-rGO structures proposed by DFT simulations reported in Fig. 3. The ARTEMIS package[43,44] was exploited to fit the data in R space within the window [0.8 − 3.2 Å] in order to include the first two coordination shells. The coordination number N was fixed by the theoretical model whereas the amplitudes (S_0^2), interatomic distances (R_i) and Debye-Waller factors ($\boldsymbol{\sigma}^2$) of the first and second atomic shells were fitted. Among the simulated structures, the one reported in Fig. 3f was the only one that fitted well the experimental data (see Fig. 4), with an R-factor of 0.7% and with a value of S_0^2 in the range of those already reported for Cu[45] and very close to the one obtained from the fitting of the Cu-foil measured as a reference.

The values of the structural parameters extracted from the curve fit for the (f) structure are reported in Table 1. Analyzing structure (f) in more details, the first broad peak in the EXAFS data, at around 1.4 Å, corresponds to the backscattering from the first four O atoms, whereas the second shell would correspond to the closest two C atoms. Scattering from H atoms is very weak and its contribution to the total EXAFS signal is negligible.

Once confirmed that the local structure around the copper atoms is well represented by the one depicted in Fig. 3f, we calculated the changes induced in the electronic properties of rGO by the presence of Cu^{2+} surface complexes. The electronic properties of this structure were analyzed in terms of density of states (DOS) and projected DOS (PDOS), as shown in Fig. 5.

The main effect induced by the Cu^{2+} complex corresponds to the appearance of occupied valence states between −10 eV and −3 eV below the Fermi level, due to the hybridization of Cu 3d orbitals with O 2p and C 2p orbitals. Cu^{2+} based complexes give rise to occupied states located right below the Fermi level that is spatially localized on the O atoms directly bound to Cu atom. The observed increase of the density of occupied states near the Fermi level indicates that these complexes behave as an n-type dopant and increase the sample conductivity as discussed below.

Electrochemical characterizations

The electrocatalytic performance of Cu-N-rGO was evaluated in an alkaline solution with dissolved oxygen from the air at ambient

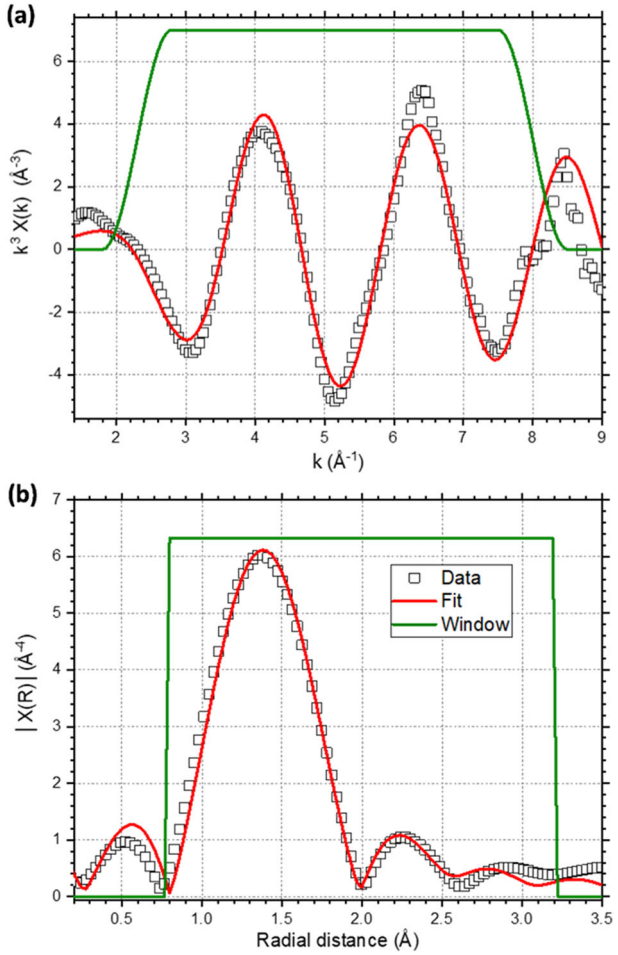

Fig. 4 EXAFS study of Cu-N-rGO sample. a k^3-weighted Cu K edge EXAFS, **b** corresponding Fourier transform in *R*-space. The solid red lines represent the best fit obtained using the structure of Fig. 3f.

Table 1. EXAFS fitting[a] parameters for structure (f).

Shell	S_0^2	R_i	σ^2_1	*R*-factor
Cu-O_1	0.84 ± 0.18	1.89 ± 0.02	0.0025 ± 0.0015	0.007
Cu-O_2		1.94 ± 0.02	0.0025 ± 0.0015	
Cu-C_1		2.59 ± 0.10	0.016 ± 0.011	
Cu-C_2		2.76 ± 0.10	0.016 ± 0.011	

[a]The coordination number was fixed by the theoretical model whereas the amplitudes (S_0^2), interatomic distances (R_i) and Debye-Waller factors (σ^2) were fitted. R_i is distance between the Cu and the different backscattering shells; σ^2 encapsulates static and thermal disorder; and the R-factor indicates the quality of the fit. Fitting ranges were 2.3–8 $Å^{-1}$ in k, and 0.8–3.2 Å in *R*.

conditions. N-rGO and a commercial Pt/C were also studied for comparison.

Cyclic voltammetry was initially carried out in 0.1 M KOH solution with nitrogen or air purging. In N_2-saturated electrolyte, both Cu-N-rGO and N-rGO samples show supercapacitor performance, evident from the characteristic quasi-rectangular voltammogram (Fig. 6), which is typical of high-surface-area carbons[46]. It is worth noting that a pair of redox peaks appears in the Cu-N-rGO voltammogram at 0.91 V in the anodic direction and 0.71 V in the cathodic direction, which are related to the formation and

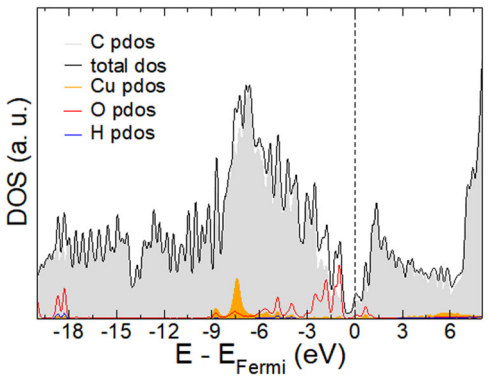

Fig. 5 Analysis of electronic properties of Cu-N-rGO sample. Density of states (DOS) and projected density of states (PDOS) for Cu-N-rGO in the configuration reported in Fig. 3f. The black lines correspond to the total DOS, the grey lines to the DOS projected on C atoms, the orange line to DOS projected on Cu atom, blue and red lines represent the DOS projected on H and O atoms respectively; the thin dashed vertical line corresponds to the position of Fermi Energy.

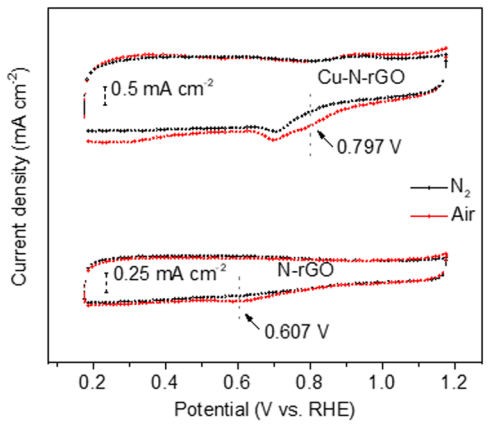

Fig. 6 Cyclic voltammetry analysis. Cyclic voltammograms of graphene-based catalysts in air- and N_2-saturated 0.1 M KOH solutions.

reduction of metal-OH_{ads}, respectively[47]. It was also stated[47] that the redox of such metal sites promotes the ORR and simultaneously maintains the catalytic cycle stable in alkaline media. When the electrolyte is purged with air, a well-defined cathodic peak appears in the voltammograms, centered at 0.61 V for N-rGO and 0.80 V for Cu-N-rGO, indicating that both samples are active for ORR even at low oxygen concentration. It is widely accepted that the catalytic properties of N-doped carbons are ascribed to the doping-induced charge delocalization or to the spin distribution alteration of the sp^2 carbon plane, which facilitate the oxygen adsorption and subsequent O–O bond cleavage[17,48–50]. This change in the electron density induced by nitrogen species can improve the electrical properties of N-doped graphene[51] and create active sites for ORR[52]. The Cu functionalization of N-rGO has further enhanced the catalytic activity for ORR, as evidenced by a positive shift of the reductive peak by 190 mV with respect to the bare N-rGO.

To further characterize the ORR activity of the prepared materials, rotating disk electrode measurements were performed. By drawing tangent lines from the rising current and baseline current in the linear sweep voltammograms, we can obtain an intersection where the potential is considered onset potential (E_{onset})[53]. As shown in Fig. 7, the E_{onset} of the ORR is 0.80 V for N-rGO and 0.91 V for Cu-N-rGO. The E_{onset} at the Cu-N-rGO

electrode indicates a minimum activation overpotential of 0.32 V for the four-electron ORR, slightly higher than 0.29 V at commercial Pt/C catalysts in alkaline solutions[17,54,55]. In addition, the Cu-N-rGO also shows a good half-wave potential ($E_{1/2}$) of 0.78 V. The high performance of Cu-N-rGO could be related to the rich Cu^{2+} active sites, whose electron density is tuned by the connection with residual oxygen atoms present in the graphene lattice, as confirmed by EXAFS, XPS analysis and DFT simulations. In addition, the mass-transfer-limited current density of Cu-N-rGO is twice that of N-rGO electrode, which could be due to the positive kinetic effect as well as high mass diffusion rate on the former.

Electrochemical impedance spectroscopy analysis was carried out in order to further identify the rationale of the different behavior. In agreement with the results presented above, the N-rGO sample exhibits larger total impedance values with respect to the Cu-containing material, as shown in Fig. 8. The experimental data were fitted with the equivalent circuit shown in the inset of Fig. 8. The series resistance R_s accounts for the electrolyte and

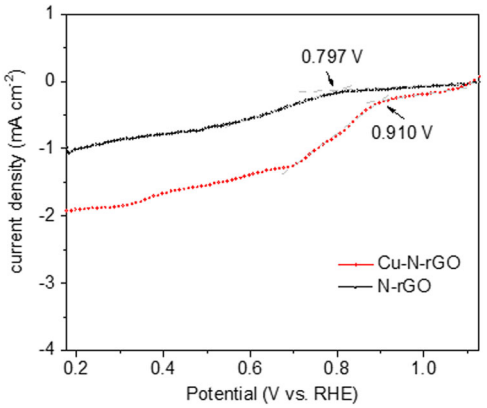

Fig. 7 Linear sweep voltammetry analysis. Linear sweep voltammograms on graphene-based catalysts in air-saturated 0.1 M KOH solution.

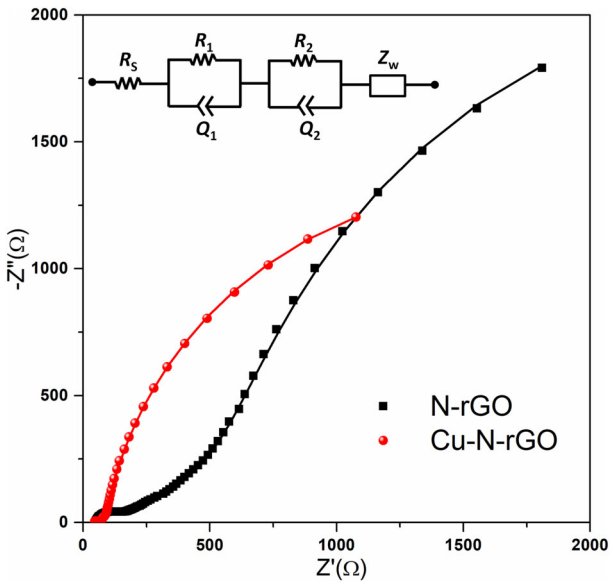

Fig. 8 Electrochemical impedance spectroscopy analysis. Electrochemical impedance spectroscopy measurements on graphene-based catalysts in air-saturated 0.1 M KOH solution. The points are experimental data, the continuous lines are the curves simulated exploiting the equivalent circuit shown in the inset.

wiring resistances, the parallels $R_1//Q_1$ and $R_2//Q_2$ model the charge transport and transfer processes inside the catalyst and at the catalyst/electrolyte interface, respectively, and the Warburg element W represents the diffusion of ionic species[9,56,57]. It is worth noting that constant phase elements (with exponent in the range of 0.85–0.95) were used instead of capacitances to take into account frequency dispersion due to the porous nature of the catalyst materials[58]. Very large capacitances (54 and 68 mF cm^{-2} for N-rGO and Cu-N-rGO, respectively) were obtained for these materials, confirming the supercapacitive properties of both samples. As expected, series and diffusion resistances (about 47 Ω and 18 Ω, respectively) are similar for the two samples, while larger differences were obtained for the other resistances. In particular, Cu-N-rGO exhibits an R_1 value equal to 70 Ω, which is smaller than that of N-rGO sample (82 Ω), confirming that the presence of Cu^{2+}-based complexes is effective in increasing the material conductivity, as suggested by the presence of occupied states near the Fermi level discussed above. In addition, the charge transfer at the interface is also enhanced for the Cu-N-rGO catalyst, as evidenced by the lower R_2 value of 3098 Ω with respect to 4315 Ω for the N-rGO sample. The availability of electrons at the Fermi energy or equivalently the high electrical conductivity of the catalyst largely influence the ORR mechanism[18]. On the Cu-N-rGO catalyst, sufficient electron density could promote coupled proton-electron transfer with lower barriers for ORR with respect to the uncoupled steps[59]. Hence, we believe that the good conductivity plays a crucial role in the high activity of the Cu-N-rGO for the ORR, as evidenced by low activation overpotential, good half-wave potential, and high current density in air ambient.

Beside the catalytic activity, the pathway of the ORR is another important criterion for evaluating an electrocatalyst. As is well known, the ORR can proceed through a two-electron process (reaction 1) or a four-electron process (reaction 2) in alkaline conditions (pH larger than 11.7)[18,60]:

$$O_2 + H_2O + 2e^- \rightarrow HO_2^- + OH^- \quad U^0 = 0.76\,V \text{ vs. RHE} \quad \text{(reaction 1)}$$
$$O_2 + H_2O + 4e^- \rightarrow 4OH^- \quad U^0 = 1.23\,V \text{ vs. RHE} \quad \text{(reaction 2)}$$

where U^0 is the standard potential for the reactions. Generally, peroxide formation through two-electron ORR is undesirable, since it not only lowers the maximum attainable voltage, thus decreasing the efficiency, but also causes chemical degradation of electrodes and other components of the electrochemical devices due to its corrosive nature[61]. The rotating ring disk electrode technique provides a fast way to obtain the number of transferred electrons and the percentage of produced peroxide as a function of the applied potential at the disk electrode, as displayed in Fig. 9.

The ORR on Cu-N-rGO sample follows a quasi four-electron pathway producing less than 5% peroxide, which is comparable to the performance of a commercial Pt/C in the observed potential

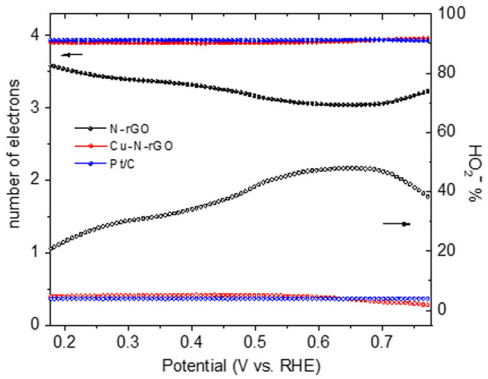

Fig. 9 Rotating ring disk electrode study. Number of electrons (left axis) and peroxide percentage (right axis) on graphene-based and reference Pt/C catalysts in air-saturated 0.1 M KOH solution.

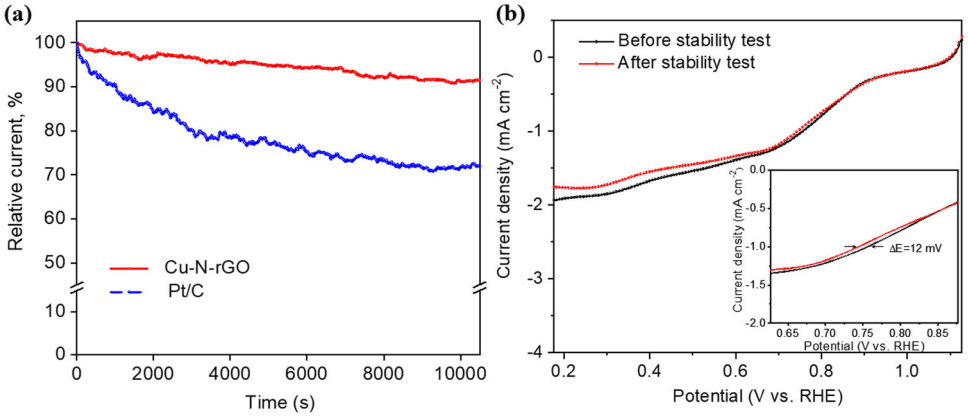

Fig. 10 Stability tests. a CA measurements on Cu-N-rGO and reference Pt/C catalysts in air-saturated 0.1 M KOH solution, **b** linear sweep voltammograms on Cu-N-rGO before and after the CA test (the inset shows the high magnification in the 0.63–0.89 V range).

window, and similar to other graphene-based electrocatalysts[62–64]. On the contrary, the N-rGO catalyst exhibits the coexistence of two- and four-electron processes, with 30–50% peroxide produced. The enhanced efficiency of Cu-N-rGO could be due to the redox Cu^{2+} species, which ensures direct O_2 adsorption on the copper-based active site and leads to four-electron electrocatalytic inner-sphere electron transfer[47].

Chronoamperometric (CA) tests at 0.68 V were performed to evaluate the electrochemical stability of Cu-N-rGO catalyst for ORR. Linear sweep voltammograms were acquired also before and after CA test through rotating disk electrode measurements. As displayed in Fig. 10a, Cu-N-rGO maintains a higher current percentage during the CA tests compared to the commercial Pt/C catalyst. Moreover, it shows a small decrease (8 %) of current density and a slightly negative shift (±12 mV) of $E_{1/2}$ after the long-term test (Fig. 10b). This indicates a very good stability, comparable to that of transition metal catalysts protected by a carbon shell against surface segregation or oxidation when exposed to oxygen or water[55]. The slight decrease of the activity of the graphene-based catalyst can be attributed to the oxidative attack of the ORR intermediates or to the demetalation of the metal-active site[65]. It is important to highlight that the electrochemical performance exhibited by the herein proposed Cu-N-rGO is in line or even better with respect to that of other reported 2D-based ORR catalysts in terms of onset and half-wave potentials, number of transferred electrons, long-term stability, as summarized in Supplementary Table 1.

DISCUSSION

In this work, we reported a rGO-based catalyst for ORR and elucidated the structure of the active sites as well as the structure-preformation correlation. By combining XPS and EXAFS characterizations with DFT calculations, we understood that our synthesis method generates Cu^{2+} ions coordinated to residual oxygen atoms present on the rGO surface and to hydroxyl groups coming from the precursor solution. The Cu ions are identified to play a determining role in efficiently driving the ORR by increasing the material conductivity and enhancing the charge transfer at catalyst/electrolyte interface. In addition, the redox Cu^{2+} species ensures direct O_2 adsorption at the active site and leads to the desired four-electron ORR pathway.

In conclusion, the coordinated copper ions have imparted to N-rGO high catalytic activity and brilliant long-term stability for ORR, outperforming noble metal-containing catalysts. Particularly, the present work highlights that, thanks to a fast and green microwave-assisted process, it is possible to synthesize unconventional high-performance catalysts, aiming at application in a wide range of challenging electrochemical reactions such as ORR, water splitting and CO_2 reduction.

METHODS

Synthesis of the catalysts

All chemicals were used as purchased without further purification. N-rGO and Cu-N-rGO catalysts were fabricated through a modified procedure reported by El-Deen et al.[66].

In a typical synthesis, 50 mg of GO (Single Layer Graphene Oxide, Cheap Tubes Inc., USA, product number 060102) was suspended in 30 mL of double distilled water containing 20 mg of urea (Urea ACS reagent, 99.0–100.5%, Sigma-Aldrich, product number U5378-100G). In the case of Cu-N-rGO sample, 25 mg of $CuSO_4{\cdot}5H_2O$ (Copper (II) sulfate pentahydrate ACS reagent, ≥98.0%, Sigma-Aldrich, product number 209198-100G) was added and dissolved in the as-prepared suspension. For both samples, the precursor mixtures were sonicated for 40 min and then transferred in a 100 mL Teflon reactor, equipped with pressure and temperature probes and placed in the microwave furnace (Milestone STARTSynth, Milestone Inc., Shelton, Connecticut). The mixtures were irradiated for 15 min at 180 °C (max. 800 W) and then the reactor was cooled to ambient temperature. The final powder samples were obtained by freeze-drying (Lio-5P, 5Pascal, Italy).

Physical and chemical characterizations

Field emission scanning electron microscopy (ZEISS Dual Beam Auriga) was used to evaluate the morphology of the studied material. Transmission electron microscopy (FEI Tecnai F20ST, 200 kV) and energy dispersive X-ray spectroscopy (EDX, EDAX) were used to evaluate the morphology, structure and composition of the studied material. High-angle annular dark field (HAADF) detector was used in Scanning TEM (STEM) mode. Samples for TEM analysis were prepared by suspending the obtained nanocomposite powder in ethanol and then dropping the suspension on a TEM Au grid with holey carbon film. The Au grid was used to avoid detection of spurious Cu signal not related to the sample.

A PHI 5000 Versaprobe Scanning X-ray Photoelectron Spectrometer was used to investigate the material chemical composition. The X-ray source was a monochromatic Al Kα radiation (1486.6 eV). The spectra were analyzed using CasaXPS Version 2.3.18 dedicated software. All core-level peak energies were referenced to the C 1s peak at 284.5 eV and the background contribution, in high resolution (HR) spectra, was subtracted by means of a Shirley function.

The Cu K-edge EXAFS measurements were performed at room temperature in transmission mode on the beamline ID16B at the ESRF[41]. The sample powder was deposited on a $5 \times 5 \times 0.5\ mm^3$ window closed with 8 µm-thick kapton. The incident flux was measured by an ion chamber filled with N_2 and the transmitted flux by a 500 µm-thick Si diode. The size of the beam was $1 \times 1\ mm^2$ and the X-ray energy was scanned around the Cu K edge between 8.8 keV and 9.6 keV with 1 eV step size and 200 ms counting time per point. Apart from the Cu-N-rGO sample, a Cu metallic foil was also measured as a reference. The analysis of the EXAFS was performed with the Athena and Artemis packages[43] using FEFF and

IFFEFIT[44]. The theoretical backscattering amplitudes and phase shifts for single and multiple scattering of the different structures were obtained using FEFF[44]. Artemis was then used to fit the theoretical values to the experimental data.

Computational details

All theoretical calculations are based on spin-polarized density functional theory as implemented in the Quantum Espresso package[67]. The Kohn-Sham equations are solved using ultrasoft pseudopotential to describe the electron-ion interaction, employing the gradient-corrected Perdew-Burke-Ernzerhof (PBE) functional[68] to describe the exchange-correlation effects, and expanding the electronic wave functions in plane waves (PW). To include London dispersion interactions, the DFT-D2 method proposed by Grimme[69] was used. For all calculations, a PW energy cutoff of 28 Ry for the wave functions and 280 Ry for the charge density and potentials, were adopted. 7×7 graphene supercells were employed to investigate Cu functionalization. A vacuum region of 10 Å thickness was added in the cells to avoid spurious interaction between periodic replicas. The Brillouin Zone was sampled employing a $2 \times 2 \times 1$ Monkhorst-Pack mesh[70]. All the structures were relaxed by minimizing the atomic forces and convergence was assumed when the maximum component of the residual forces on the ions was smaller than 10^{-4} Ry/Bohr. To partially heal the underestimation of the energy gap typical of PBE when applied to transition metals, such as Cu, we applied to the relaxed structures a Hubbard U correction to the Cu-3d orbital ($U_{Cu} = 11.50$ eV) obtained following the procedure reported in ref. [71].

Electrochemical characterizations

All electrochemical characterizations were performed at room temperature with a CHI760D electrochemical workstation and an ALS RRDE−3A rotating ring disk electrode apparatus. The catalyst samples were deposited onto the glassy carbon (GC) disk (electrode area 0.1256 cm^2) of GC disk/Pt ring working electrode following the procedure reported in ref. [9]. A Pt wire was used as counter electrode and Ag/AgCl was used as reference electrode. Unless otherwise specified, all the measurements were carried out in a 3-electrode configuration (disk working/reference/counter electrodes) in air-saturated 0.1 M KOH aqueous electrolytic solution (Potassium hydroxide concentrate, 0.1 M KOH in water (0.1 N), Supelco, product number 61699-1L) with 2500 RPM rotation speed, and all potentials refer to the RHE. A reference Pt/C catalyst (Pt/C, 10 wt. % Pt loading, matrix activated carbon support, Sigma Aldrich, product number 205958-10G) was used to compare the obtained result with a commercially available material.

Cyclic voltammetry curves were acquired from 1.18 V to 0.18 V with a scan rate of 10 mV/s in air- and N_2-saturated electrolytic solution. Rotating disk electrode tests were carried out in the potential range 1.18 V–0.18 V with a scan rate of 5 mV/s. Electrochemical impedance spectroscopy measurements were performed at fixed 0.68 V potential, with an AC signal of 10 mV amplitude and 10^{-2}–10^4 Hz frequency range. Chronoamperometric (CA) data were acquired at fixed 0.68 V potential. Rotating ring disk electrode measurements were carried out in a 4-electrode configuration (disk and ring working/reference/counter electrodes) by applying linear sweep voltammetry at the disk electrode from 1.18 V to 0.18 V (at a scan rate of 5 mV/s) and by employing controlled-potential CA on the ring potential at 1.18 V. The measured disk (I_D) and ring (I_R) currents were employed to calculate the number of transferred electrons (n) and the percentage of produced peroxide (HO_2^-%) according to the formulae:

$$n = 4 \cdot \frac{I_D}{I_D + \frac{I_R}{N}} \quad (1)$$

$$HO_2^-\% = 200 \cdot \frac{\frac{I_R}{N}}{I_D + \frac{I_R}{N}} \quad (2)$$

where N is the current collection efficiency of the ring electrode[56].

DATA AVAILABILITY

All data generated or analyzed during this study are included in this published article (and its Supplementary information file).

Received: 4 August 2020; Accepted: 25 November 2020;
Published online: 04 January 2021

REFERENCES

1. Sharaf, O. Z. & Orhan, M. F. An overview of fuel cell technology: fundamentals and applications. *Renew. Sustain. Energy Rev.* **32**, 810–853 (2014).
2. Pivovar, B. Catalysts for fuel cell transportation and hydrogen related uses. *Nat. Catal.* **2**, 562–565 (2019).
3. Wang, H.-F. & Xu, Q. Materials design for rechargeable metal-air batteries. *Matter* **1**, 565–595 (2019).
4. Imanishi, N. & Yamamoto, O. Perspectives and challenges of rechargeable lithium-air batteries. *Mater. Today Adv.* **4**, 100031 (2019).
5. Li, Y. & Lu, J. Metal-air batteries: will they be the future electrochemical energy storage device of choice? *ACS Energy Lett.* **2**, 1370–1377 (2017).
6. Chen, M., He, Y., Spendelow, J. S. & Wu, G. Atomically dispersed metal catalysts for oxygen reduction. *ACS Energy Lett.* **4**, 1619–1633 (2019).
7. Katsounaros, I., Cherevko, S., Zeradjanin, A. R. & Mayrhofer, K. J. J. Oxygen electrochemistry as a cornerstone for sustainable energy conversion. *Angew. Chem. Int. Ed.* **53**, 102–121 (2014).
8. Wang, X. et al. Review of metal catalysts for oxygen reduction reaction: from nanoscale engineering to atomic design. *Chem.* **5**, 1486–1511 (2019).
9. Garino, N. et al. Microwave-assisted synthesis of reduced graphene oxide/SnO_2 nanocomposite for oxygen reduction reaction in microbial fuel cells. *ACS Appl. Mater. Interfaces* **8**, 4633–4643 (2016).
10. Chen, M. et al. Nanocarbon/oxide composite catalysts for bifunctional oxygen reduction and evolution in reversible alkaline fuel cells: A mini review. *J. Power Sources* **375**, 277–290 (2018).
11. Zhao, X. et al. Controlled fabrication of hierarchically structured nitrogen-doped carbon nanotubes as a highly active bifunctional oxygen electrocatalyst. *Adv. Funct. Mater.* **27**, 1605717 (2017).
12. Zeng, J. et al. Mesoporous Co_3O_4 nanocrystals as an effective electro-catalyst for highly reversible Li–O_2 batteries. *J. Power Sources* **272**, 1003–1009 (2014).
13. Singh, H., Zhuang, S., Ingis, B., Nunna, B. B. & Lee, E. S. Carbon-based catalysts for oxygen reduction reaction: A review on degradation mechanisms. *Carbon* **151**, 160–174 (2019).
14. Ma, R. et al. A review of oxygen reduction mechanisms for metal-free carbon-based electrocatalysts. *Npj Comput. Mater.* **5**, 78 (2019).
15. Wu, G. Current challenge and perspective of PGM-free cathode catalysts for PEM fuel cells. *Front. Energy* **11**, 286–298 (2017).
16. Thompson, S. T. et al. ElectroCat: DOE's approach to PGM-free catalyst and electrode R&D. *Solid State Ion.* **319**, 68–76 (2018).
17. Lemes, G., Sebastián, D., Pastor, E. & Lázaro, M. J. N-doped graphene catalysts with high nitrogen concentration for the oxygen reduction reaction. *J. Power Sources* **438**, 227036 (2019).
18. Kim, H. W. et al. Mechanisms of two-wlectron and four-electron electrochemical oxygen reduction reactions at nitrogen-doped reduced graphene oxide. *ACS Catal.* **10**, 852–863 (2020).
19. Wang, L. et al. Potential application of novel boron-doped graphene nanoribbon as oxygen reduction reaction catalyst. *J. Phys. Chem. C.* **120**, 17427–17434 (2016).
20. Ma, Z. et al. Nanoscale trimetallic metal-organic frameworks enable efficient oxygen evolution electrocatalysis. *Angew. Chem. Int. Ed.* **54**, 1888–1892 (2015).
21. Zhang, C., Mahmood, N., Yin, H., Liu, F. & Hou, Y. Synthesis of phosphorus-doped graphene and its multifunctional applications for oxygen reduction reaction and lithium ion batteries. *Adv. Mater.* **25**, 4932–4937 (2013).
22. Jeon, I.-Y. et al. Facile, scalable synthesis of edge-halogenated graphene nanoplatelets as efficient metal-free eletrocatalysts for oxygen reduction reaction. *Sci. Rep.* **3**, 1810 (2013).
23. Fernandes, D. M., Mathumba, P., Fernandes, A. J. S., Iwuoha, E. I. & Freire, C. Towards efficient oxygen reduction reaction electrocatalysts through graphene doping. *Electrochim. Acta* **319**, 72–81 (2019).
24. Tabassum, H., Zou, R., Mahmood, A., Liang, Z. & Guo, S. A catalyst-free synthesis of B, N co-doped graphene nanostructures with tunable dimensions as highly efficient metal free dual electrocatalysts. *J. Mater. Chem. A* **4**, 16469–16475 (2016).
25. Wu, D., Wang, T., Wang, L. & Jia, D. Hydrothermal synthesis of nitrogen, sulfur co-doped graphene and its high performance in supercapacitor and oxygen reduction reaction. *Micropor. Mesopor. Mater.* **290**, 109556 (2019).
26. Li, R., Wei, Z. & Gou, X. Nitrogen and phosphorus dual-doped graphene/carbon nanosheets as bifunctional electrocatalysts for oxygen reduction and evolution. *ACS Catal.* **5**, 4133–4142 (2015).
27. Ma, R. et al. Ionic liquid-assisted synthesis of dual-doped graphene as efficient electrocatalysts for oxygen reduction. *Carbon* **102**, 58–65 (2016).

28. Lin, H. et al. Boron, nitrogen, and phosphorous ternary doped graphene aerogel with hierarchically porous structures as highly efficient electrocatalysts for oxygen reduction reaction. *N. J. Chem.* **40**, 6022–6029 (2016).
29. Molina-García, M. A. & Rees, N. V. "Metal-free" electrocatalysis: Quaternary-doped graphene and the alkaline oxygen reduction reaction. *Appl. Catal. A: Gen.* **553**, 107–116 (2018).
30. Shakhseh, B. & Seyyedi, B. Enhanced electrocatalytic performance of $Cu_{0.02}S_{0.01}$/rGO hybrid for oxygen reduction reaction in alkaline medium at low temperature. *Int. J. Hydrog. Energy* **44**, 25621–25631 (2019).
31. Noh, W. Y., Lee, J. H. & Lee, J. S. Nitrogen-doped carbon nanotube-graphene hybrid stabilizes MxN (M=Fe, Co) nanoparticles for efficient oxygen reduction reaction. *Appl. Catal. B: Environ.* **268**, 118415 (2020).
32. Sudarsono, W. et al. Noble-free oxygen reduction reaction catalyst supported on Sengon wood (Paraserianthes falcataria L.) derived reduced graphene oxide for fuel cell application. *Int. J. Energy Res.* **44**, 1761–1774 (2020).
33. Garino, N. et al. Proving the existence of Mn porphyrin-like complexes hosted in reduced graphene oxide with outstanding performance as oxygen reduction reaction catalysts. *2D Mater.* **6**, 045001 (2019).
34. Varga, T. et al. Co_4N/nitrogen-doped graphene: a non-noble metal oxygen reduction electrocatalyst for alkaline fuel cells. *Appl. Catal. B: Environ.* **237**, 826–834 (2018).
35. Risplendi, F., Re Fiorentin, M. & Cicero, G. Unravelling electrocatalytic properties of metal porphyrin-like complexes hosted in graphene matrices. *2D Mater.* **7**, 025017 (2020).
36. Wang, J., Wang, K., Wang, F.-B. & Xia, X.-H. Bioinspired copper catalyst effective for both reduction and evolution of oxygen. *Nat. Commun.* **5**, 5285 (2014).
37. Li, F. et al. Boosting oxygen reduction catalysis with abundant copper single atom active sites. *Energy Environ. Sci.* **11**, 2263–2269 (2018).
38. Garino, N. et al. One-pot microwave-assisted synthesis of reduced graphene oxide/iron oxide nanocomposite catalyst for the oxygen reduction reaction. *ChemistrySelect* **1**, 3640–3646 (2016).
39. Biesinger, M. C. Advanced analysis of copper X-ray photoelectron spectra. *Surf. Interface Anal.* **49**, 1325–1334 (2017).
40. Beamson, G. & Briggs, D. High Resolution XPS of Organic Polymers-The Scienta ESCA300 Database. Wiley Interscience, Appendices 3.1 and 3.2 (1992).
41. Martinez-Criado, G. et al. ID16B: a hard X-ray nanoprobe beamline at the ESRF for nano-analysis. *J. Synchrotron Radiat.* **23**, 344–352 (2016).
42. Ankudinov, A. L., Ravel, B., Rehr, J. J. & Conradson, S. D. Real-space multiple-scattering calculation and interpretation of x-ray-absorption near-edge structure. *Phys. Rev. B* **58**, 7565–7576 (1998).
43. Ravel, B. & Newville, M. ATHENA, ARTEMIS, HEPHAESTUS: data analysis for X-ray absorption spectroscopy using IFEFFIT. *J. Synchrotron Radiat.* **12**, 537–541 (2005).
44. Newville, M. IFEFFIT: interactive XAFS analysis and FEFF fitting. *J. Synchrotron Radiat.* **8**, 322–324 (2001).
45. Li, G. G., Bridges, F. & Booth, C. H. X-ray-absorption fine-structure standards: A comparison of experiment and theory. *Phys. Rev. B* **52**, 6332–6348 (1995).
46. Fellinger, T.-P., Hasché, F., Strasser, P. & Antonietti, M. Mesoporous nitrogen-noped carbon for the electrocatalytic synthesis of hydrogen peroxide. *J. Am. Chem. Soc.* **134**, 4072–4075 (2012).
47. Ramaswamy, N., Tylus, U., Jia, Q. & Mukerjee, S. Activity descriptor identification for oxygen reduction on nonprecious electrocatalysts: linking surface science to coordination chemistry. *J. Am. Chem. Soc.* **135**, 15443–15449 (2013).
48. Choi, C. H., Park, S. H. & Woo, S. I. Binary and ternary doping of nitrogen, boron and phosphorus into carbon for enhancing electrochemical oxygen reduction activity. *ACS Nano* **6**, 7084–7091 (2012).
49. Tang, C. & Zhang, Q. Nanocarbon for oxygen reduction electrocatalysis: dopants, edges, and defects. *Adv. Mater.* **29**, 1604103 (2017).
50. Xing, T. et al. Observation of active sites for oxygen reduction reaction on nitrogen-doped multilayer graphene. *ACS Nano* **8**, 6856–6862 (2014).
51. Daems, N. et al. Doped ordered mesoporous carbons as novel, selective electrocatalysts for the reduction of nitrobenzene to aniline. *J. Mater. Chem. A* **6**, 13397–13411 (2018).
52. Zheng, Y., Jiao, Y., Jaroniec, M., Jin, Y. & Qiao, S. Nanostructured metal-free electrochemical catalysts for highly efficient oxygen reduction. *Small* **8**, 3550–3566 (2012).
53. Tran, T.-N., Song, M. Y., Singh, K. P., Yang, D.-S. & Yu, J.-S. Iron-polypyrrole electrocatalyst with remarkable activity and stability for ORR in both alkaline and acidic conditions: a comprehensive assessment of catalyst preparation sequence. *J. Mater. Chem. A* **4**, 8645–8657 (2016).
54. Yang, S. et al. Efficient synthesis of heteroatom (N or S)-doped graphene based on ultrathin graphene oxide-porous silica sheets for oxygen reduction reactions. *Adv. Funct. Mater.* **22**, 3634–3640 (2012).
55. Noh, S. H. et al. Design of an active and durable catalyst for oxygen reduction reactions using encapsulated Cu with N-doped carbon shells (Cu@N-C) activated by CO_2 treatment. *J. Mater. Chem. A* **3**, 22031–22034 (2015).
56. Delmondo, L. et al. Nanostructured Mn_xO_y for oxygen reduction reaction (ORR) catalysts. *Appl. Surf. Sci.* **388, Part B**, 631–639 (2016).
57. Orazem, M. E. & Tribollet, B. *Electrochemical Impedance Spectroscopy*, 2nd Edition (Wiley, 2008).
58. Hernández, S. et al. New transparent laser-drilled fluorine-doped tin oxide covered quartz electrodes for photo-electrochemical water splitting. *Electrochim. Acta* **131**, 184–194 (2014).
59. Koper, M. T. M. Theory of multiple proton–electron transfer reactions and its implications for electrocatalysis. *Chem. Sci.* **4**, 2710–2723 (2013).
60. Kim, W. S. et al. Facile synthesis of perovskite $LaMnO_{3+\delta}$ nanoparticles for the oxygen reduction reaction. *J. Catal.* **344**, 578–582 (2016).
61. Dumitrescu, I. & Crooks, R. M. Effect of mass transfer on the oxygen reduction reaction catalyzed by platinum dendrimer encapsulated nanoparticles. *Proc. Nat. Acad. Sci.* **109**, 11493–11497 (2012).
62. Bai, X. et al. Catalytic activities enhanced by abundant structural defects and balanced N distribution of N-doped graphene in oxygen reduction reaction. *J. Power Sources* **306**, 85–91 (2016).
63. Pan, F., Jin, J., Fu, X., Liu, Q. & Zhang, J. Advanced oxygen reduction electrocatalyst based on nitrogen-doped graphene derived from edible sugar and urea. *ACS Appl. Mater. Interfaces* **5**, 11108–11114 (2013).
64. Vikkisk, M. et al. Electrocatalytic oxygen reduction on nitrogen-doped graphene in alkaline media. *Appl. Catal. B: Environ.* **147**, 369–376 (2014).
65. Singh, H., Zhuang, S., Ingis, B., Nunna, B. B. & Lee, E. S. Carbon-based catalysts for oxygenreduction reaction: A review on degradation mechanisms. *Carbon* **151**, 160–174 (2019).
66. El-Deen, A. G., Barakat, N. A. M., Khalil, K. A., Motlak, M. & Kim, H. Y Graphene/SnO_2 nanocomposite as an effective electrode material for saline water desalination using capacitive deionization. *Ceram. Int.* **40**, 14627–14634 (2014).
67. Giannozzi, P. et al. QUANTUM ESPRESSO: a modular and open-source software project for quantum simulations of materials. *J. Phys.: Cond. Matt.* **21**, 395502 (2009).
68. Perdew, J. P., Burke, K. & Wang, Y. Generalized gradient approximation for the exchange-correlation hole of a many-electron system. *Phys. Rev. B* **54**, 16533–16539 (1996).
69. Grimme, S. Semiempirical GGA-type density functional constructed with a long-range dispersion correction. *J. Comput. Chem.* **27**, 1787–1799 (2006).
70. Monkhorst, H. J. & Pack, J. D. Special points for Brillouin-zone integrations. *Phys. Rev. B* **13**, 5188–5192 (1976).
71. Cococcioni, M. & de Gironcoli, S. Linear response approach to the calculation of the effective interaction parameters in the LDA+U method. *Phys. Rev. B* **71**, 035105 (2005).

ACKNOWLEDGEMENTS

The CINECA award under the ISCRA initiative and HPC@ POLITO are acknowledged for the availability of high performance computing resources and support. The ESRF is acknowledged for the beamtime allocated.

AUTHOR CONTRIBUTIONS

N.G. and J.Z. contributed equally to this work and are considered "co-first author". J.Z., A.S., N.G., and G.C. contributed to the conceptualization. C.F.P. contributed to the resources. J.Z., N.G., and A.S. contributed to the synthesis and electrochemical measurements. M.C. contributed to the XPS investigation. K.B. and A.C. contributed to FESEM and TEM investigations. F.R., M.R.F., and G.C. contributed to the DFT calculations. D.S. and J.S.-R. contributed to the Extended X-Ray Absorption Fine Structure (EXAFS) analysis. All authors contributed to the manuscript composition.

COMPETING INTERESTS

The authors declare no competing interests.

ADDITIONAL INFORMATION

Supplementary information is available for this paper at https://doi.org/10.1038/s41699-020-00185-x.

Correspondence and requests for materials should be addressed to N.G. or J.Z.

Reprints and permission information is available at http://www.nature.com/reprints

Publisher's note Springer Nature remains neutral with regard to jurisdictional claims in published maps and institutional affiliations.

Open Access This article is licensed under a Creative Commons Attribution 4.0 International License, which permits use, sharing, adaptation, distribution and reproduction in any medium or format, as long as you give appropriate credit to the original author(s) and the source, provide a link to the Creative Commons license, and indicate if changes were made. The images or other third party material in this article are included in the article's Creative Commons license, unless indicated otherwise in a credit line to the material. If material is not included in the article's Creative Commons license and your intended use is not permitted by statutory regulation or exceeds the permitted use, you will need to obtain permission directly from the copyright holder. To view a copy of this license, visit http://creativecommons.org/licenses/by/4.0/.

© The Author(s) 2021